Monte Carlo simulations of the magnetic behaviour of iron oxide nanoparticle ensembles : taking size dispersion, particle anisotropy, and dipolar interactions into account

Monte Carlo Simulations of the Magnetic Behaviour of Iron Oxide Nanoparticle Ensembles: Taking Size Dispersion, Particle Anisotropy, and Dipolar Interactions Into Account

Éléonore Martin*[a], Yves Gossuin[a], Sara Bals[b], Safiyye Kavak[b], Quoc Lam Vuong[a]

November 18, 2022

*Corresponding author

[a]Biomedical Physics Unit, University of Mons, 25 avenue Maistriau, B-7000 Mons, Belgium

[b]Electron Microscopy for Materials Science (EMAT) and NANOlab Center of Excellence, University of Antwerp, B-2020 Antwerp, Belgium

Abstract

In this work, the magnetic properties of superparamagnetic iron oxide nanoparticles (SPIONs) submitted to an external magnetic field are studied using a Metropolis algorithm. The influence on the M(B) curves of the size distribution of the nanoparticles, of uniaxial anisotropy, and of dipolar interaction between the cores are examined, as well as the influence of drying the samples under a zero or non-zero magnetic field. It is shown that the anisotropy impacts the shape of the magnetization curves, which then deviate from a pure Langevin behaviour, whereas the dipolar interaction has no influence on the curves at 300K for small particles (with a radius of 3nm). The fitting of the magnetization curves of particles with magnetic anisotropy to a Langevin model (including a size distribution of the particles) can then lead to erroneous values of the distribution parameters. The simulation results are qualitatively compared to experimental results obtained for iron oxide nanoparticles (with a 3.21nm median radius).

Keywords: superparamagnetism - iron oxide nanoparticles - anisotropy - dipolar interaction - size distribution - Monte Carlo simulation

1 Introduction

1.1 Superparamagnetic Iron Oxide Nanoparticles

Since the description of superparamagnetism by Néel in 1949 [1] and then by Brown in 1963 [2], superparamagnetic iron oxide nanoparticles (SPIONs) have generated substantial interest from researchers, particularly in the field of biophysics. Their high saturation magnetization and absence of remanent magnetization make them suitable for a wide range of biomedical applications. They are used as contrast agents for magnetic resonance imaging (MRI), mostly for small animal imaging [3]. Indeed, when submitted to an external field, their magnetic moment produces local magnetic inhomogeneities which increase the relaxation rate of tissues' protons, resulting where they are present in hypointense regions in a T_2 weighted image. SPIONs also exhibit good performance and low toxicity for cell labelling and tracking [4, 5, 6, 7]. They can be used as well to aggregate and detect viruses *in vivo* through MRI [8, 9]. They are good candidates for use in cancer therapies by magnetic hyperthermia, because of the good biocompatibility of iron oxides, which degrade with low toxicity [10, 11]. They are the center of magnetic particle imaging [12, 13], magnetorelaxometry [14] (in both of which they directly generate the signal), and magnetic field assisted drug delivery [15]. Magnetite even occurs naturally in the human hippocampus, where there is still debate about its evolutionary origin and exact function. Its presence in the brain could even perhaps be correlated with neurodegenerative disease [16]. Many of these applications rely on the superparamagnetic properties of the nanoparticles. It is therefore of prime importance to fully understand their magnetic behaviour.

1.2 Langevin's model and its limitations

In 1905, Paul Langevin described paramagnetism using statistical mechanics [17], in a model that can be used as well to describe the behaviour of superparamagnetic iron oxide nanoparticles. This subsection aims at explaining that model in the context of superperamagnetism, and its limitations. The Hamiltonian of an assembly of N non-interacting, monodisperse (same-size), superparamagnetic particles without magnetic anisotropy submitted to an external field $\vec{B}$ is $H = -N\vec{\mu}\cdot\vec{B}$, where $\vec{\mu}$ is the magnetic moment of the particles in Am^2. It is proportional to their volume through the saturation magnetization M_s in A/m : $\mu = M_s V$. The saturation magnetization of bulk magnetite is around 450kA/m. In this work, the term "magnetic field" will be used for the magnetic flux density in T. Therefore, assuming the external field is applied along the z axis, the mean z-component of the total magnetic moment can be computed as :

$$\langle \mu_{tot,Z} \rangle = N \int \mu_z \frac{e^{-\frac{H(\vec{\mu})}{kT}}}{Z} d\vec{\mu} = N\mu \frac{\int_{\theta=0}^{\pi}\int_{\phi=0}^{2\pi} \cos(\theta) e^{\frac{\mu B \cos(\theta)}{kT}} \sin(\theta) d\theta d\phi}{\int_{\theta=0}^{\pi}\int_{\phi=0}^{2\pi} e^{\frac{\mu B \cos(\theta)}{kT}} \sin(\theta) d\theta d\phi} \tag{1}$$

where Z is the partition function, μ and B denote $|\vec{\mu}|$ and $|\vec{B}|$ respectively, and θ the angle separating their directions. Performing the integral yields

$$M(B) = \frac{N\mu}{V_{tot}} L\left(\frac{\mu B}{kT}\right) \tag{2}$$

where N is the number of particles, V_{tot} is their total volume, and $L(x) = \coth(x) - \frac{1}{x}$ is called the Langevin function. Reality, however, always differs from that theoretical framework:

1. In practice, the saturation magnetization of a sample of magnetite nanoparticles is always lower than 450kA/m, due, on one hand, to poor control of the oxidation level of iron during particle synthesis, which causes magnetite to oxidize to maghemite [18], and on the other hand to surface effects [19, 20].
2. SPIONs generally have at least one anisotropy axis, to which their magnetization tends to align. Anisotropy depends on the crystalline properties, the shape, and the surface of the particles. Uniaxial anisotropy, which is the simplest form of anisotropy, has been theoretically shown to impact the shape of magnetization curves [21]. For the sake of simplicity we will here limit ourselves to this case. Experimentally, to fully determine the magnetic anisotropy of a given experimental sample, it is important to ensure the sample is non-interacting [22].
3. Real particles generate a dipolar magnetic field through which they interact with each other if their concentration is high enough [23]. This is expected to impact magnetization curves. In biological media, high local concentrations occur often, as nanoparticles are internalized in endosomes [24, 25]. Moreover, in solid (i.e. dried) samples, if the coating is thin the magnetic cores are inevitably very close to one another, leading to increased interaction between particles.
4. It is impossible to produce sets of particles which all have the exact same size, and their radii inevitably present some size distribution, which is typically log-normal (sometimes, normal). Obtaining samples with narrow size distributions is a major challenge of the preparation of SPIONs. The synthesis method influences the size dispersion, non-hydrolytic paths allowing for a better control [26].

Experimentally, the particle sizes usually follow either a log-normal distribution, whose probability density function is given by

$$f_l(x) = \frac{1}{x\sigma_L\sqrt{2\pi}} e^{-\frac{(lnx-\mu_L)^2}{2\sigma_L^2}} \tag{3}$$

or (albeit less often) a normal distribution, whose probability density function is given by

$$f_n(x) = \frac{1}{\sigma_N\sqrt{2\pi}} e^{-\frac{(x-\langle x\rangle)^2}{2\sigma_N^2}} \tag{4}$$

In the log-normal distribution, $R_0 = e^{\mu}$ is the median radius of the particles. In both cases, the σ parameter is a reflection of the broadness of the size distribution. It is worth noting however that the scaling is substantially

different in the two distributions, since in the normal distribution σ_N denotes the standard deviation, but in the log-normal distribution σ_L is the standard deviation of the distribution of the *logarithms* of the radii. The particle size distribution can be taken into account by integrating equation (2) over all sizes, but without considering its interactions with the other effects at play. Notably, an integrated version of equation (2) is sometimes used to fit field-dependent curves, and extract size distribution parameters from experimental results [22, 27, 28, 29, 30, 31, 32] :

$$M(B) = \frac{1}{V_{tot}} \int f(R)\mu(R)L\left(\frac{\mu(R)B}{kT}\right) dR \tag{5}$$

where

- $f(R)$ is the probability density function of the radii,
- V_{tot} is the total volume of the magnetic cores inside the sample, which can be computed by integrating their probability density function : $V_{tot} = \int f(R)\frac{4\pi R^3}{3} dR$
- $\mu(R)$ is the particle magnetic moment, which depends on its size : $\mu = \frac{M_S 4\pi R^3}{3}$

This method of determining the size dispersion should only be used on samples containing exclusively particles in the superparamagnetic regime, i.e. particles with a radius no larger than $\sim$ 11nm at 300K for a measurement duration $\tau_M = 1$s [33]. With the distributions used in this study, no particle exhibits such a high radius.

1.3 Néel & Brown relaxation of the magnetic moment

The magnetization predicted by Langevin's theory is reached by the particles through two relaxation processes. The main one is an internal relaxation process first theorized by Néel [1]. It is a dynamical and exponential relaxation process, which is linked to their magnetocrystalline anisotropy (which we consider uniaxial), as it results from thermal agitation in the interatomic bonds of the crystal. The relaxation of the magnetization is characterized by the Néel relaxation time τ_N, given by:

$$\tau_N = \tau_0 e^{\frac{KV}{kT}} \tag{6}$$

The derivation of that time presupposes that the magnetic field is null, therefore the Hamiltonian of each particle can be reduced to

$$H = -KV\vec{1_{\mu_i}} \cdot \vec{1_{A_i}} \tag{7}$$

, with

- K is the magnetic anisotropy constant in J/cm^3;
- V is the volume of the particle in m^3;
- $\vec{1_{\mu_i}}$ the unit vector to which the particle's magnetic moment aligns;
- $\vec{1_{A_i}}$ the unit vector of the easy magnetization axis.

This is reasonable as long as the anisotropy of the material is high enough. The Néel relaxation time then represents the mean time needed for the magnetic moment of the particle to relax from one easy magnetization axis (corresponding to one minimum of the energy of the particle) to the other, under the influence of thermal agitation. The Néel relaxation time critically depends on the particle volume, but also on the temperature. Therefore, for a given sample of particles (with a fixed anisotropy constant and particle volume), there exists a certain *blocking temperature* T_B under which the typical duration of a measurement τ_M is lower than the relaxation time of the magnetic moment, i.e. $\tau_M < \tau_N$. Under the blocking temperature, thermal agitation is too weak for the energy barrier between the easy axes to be crossed regularly. As a consequence, the particles appear *blocked* as they do not have the time, over an experimental measurement, to relax between their easy magnetization axes. For magnetometric measurements of magnetite cores with a radius of 3nm, as investigated in this paper, it is typically lower than 50 K. This process is called Néel blocking. It should be stressed that Néel time depends on the applied magnetic field, and few models exist to describe the

particle relaxation under large magnetic fields. Dipolar interactions are also known to impact Néel relaxation time, and therefore can further modify the magnetic behaviour of SPIONs [23, 34]. In addition to the Néel relaxation process of the magnetic moment, in liquid samples, the particles are able to rotate, which results in modifications of the orientation of their anisotropy axis. This process is called Brown relaxation, and its characteristic relaxation time is given in the absence of a magnetic field by:

$$\tau_B = \frac{3\eta V}{kT} \tag{8}$$

where η is the viscosity of the carrier fluid [2]. In this paper, a value of 0.55mPas was used, which corresponds to various organic solvents at 300K (chloroform [35] or toluene [36] for instance). For liquid samples containing nanoparticles with a high volume fraction, the viscosity depends on the volume fraction, even for nonmagnetic particles [37]. This could influence the computation of the Brown relaxation time. Moreover, for ferrofluids, the magnetic field influences the viscosity, also at high volume fractions [38]. However, in our simulation, the volume fraction f of the liquid sample was set to 0.005. For such a low f value, those effects are expected to be negligible. Besides, in some cases, reversible clusters and chains can form in the ferrofluid under the influence of a magnetic field. This would also influence the Brown relaxation time of the cluster. Our simulations do not take this possibility into account.

1.4 Purpose of this work

The interactions of all those effects: anisotropy, dipole-dipole interactions, size distributions, are too complex to be studied purely analytically. This is where numerical simulation comes in handy: it allows to "switch on and off" the various effects. In particular, in this work, a Metropolis-Hastings algorithm is implemented, similar to previous work, such as [19, 28, 39, 40, 41], with the specificity that Brown relaxation is added in our algorithm to allow to evaluate its impact. Moreover, [28] and [39] focus on modeling one nanoparticle cluster, and [40] on particles dispersed in a solid matrix, whereas we modeled liquid and solid samples. Reference [19] does not provide a comparison with experimental results, nor a complete analysis of the impacts of the various deviations from the Langevin behaviour, which we attempt to develop in this article. Whenever possible, the simulations were compared to experimental results. The influence of the deviations from Langevin theory, in particular those caused by anisotropy, on the size distribution parameters obtained by fitting the curves to equation (5) is also probed, so as to evaluate the validity of the parameters obtained from those fits. Because of the influence of effects beyond Langevin behaviour, those fits perform poorly on real samples.

2 Materials and methods

2.1 Simulations

The initial configuration of the particles is defined by:

1. their position;
2. the orientation of their magnetic moment;
3. the orientation of their easy axis.

The positions are generated at random, but respecting a chosen volumic fraction f of magnetic cores in the simulation space, defined as

$$f = \frac{\sum_i V_i}{V_\mathrm{S}} \tag{9}$$

where V_i the volume of particle i and V_S the total volume of the simulation space. Depending on the simulation, the initial orientations of the easy axes are generated either at random or all in one given direction (in the results section of this paper, their orientation is systematically specified), and the initial orientations of the magnetic moments are always generated at random. Once the simulation space is created, the numerical simulation consists in a Metropolis-Hastings algorithm [42], which is a Monte Carlo algorithm allowing the computation of the equilibrium properties of systems. In our particular case, it translates as such:

1. A random particle in the sample is chosen, and a new magnetic moment, random in orientation, is chosen for this particle.
2. The total energy change ΔE resulting from switching to the new moment is computed. In this work, the total energy of the particle with index i (and volume V_i, and magnetic moment $\overrightarrow{\mu_i}$) comprises
   - The Zeeman interaction between the particle's magnetic moment and the external field
   $$E_i^Z = -\overrightarrow{\mu_i} \cdot \overrightarrow{B}; \tag{10}$$
   - The dipolar interaction between the particle's magnetic moment and those of its nearest neighbours :
   $$E_i^D = -\frac{\mu_0}{4\pi} \sum_j \left[\frac{3\left(\overrightarrow{\mu_i} \cdot \overrightarrow{r_{ij}}\right)\left(\overrightarrow{\mu_j} \cdot \overrightarrow{r_{ij}}\right)}{r_{ij}^5} - \frac{\overrightarrow{\mu_i} \cdot \overrightarrow{\mu_j}}{r_{ij}^3} \right] \tag{11}$$
   with j denoting the indexes of the nearest neighbours of particle i and $\overrightarrow{r_{ij}}$ the vector that goes from the center of particle j to the center of particle i. The nearest neighbours of particle i are defined as the particles within a sphere of radius R_C around particle i. R_C is called the cutoff radius of the dipolar interaction, and was chosen at five times the mean interparticle distance, after performing tests to ensure this approximation did not skew the results (see fig. S1). For the computation of the dipolar interaction, the simulation space is considered periodic, meaning that the particles on one side of the simulation space can be influenced by the particles on the other side.
   - The magnetic anisotropy of the particle, which we consider uniaxial. The magnetic anisotropy energy is given by
   $$E_i^A = KV_i \overrightarrow{1_{\mu_i}} \cdot \overrightarrow{1_{A_i}}. \tag{12}$$
   An anisotropy constant $K = 13600\mathrm{J/m^3}$, typical of magnetite (whose experimental constants typically range from 10000 to 20000 $\mathrm{J/m^3}$ [22]), is always considered here. The higher order anisotropy constants are neglected.
3. The new moment is accepted with probability $\min[e^{-\frac{\Delta E}{kT}}, 1]$.
4. The same process is repeated for the rotation of the (same) particle, which is modelled as a change of its anisotropy axis: a random new orientation of the axis is chosen, the resulting change in the energy of the sample, resulting purely from the magnetic anisotropy term, is computed, and the new axis is accepted with probability $\min[e^{-\frac{\Delta E}{kT}}, 1]$ *if the Brown time of the particle is lower than 1 second*, as this is our measurement time. Below the fusion temperature of the carrier liquid, the anisotropy axis is blocked.

This procedure is repeated without the magnetization being recorded for a certain number of so-called *equilibration steps*, and then the mean magnetization of the sample is computed over a (higher) number of steps. Our simulations also allow to consider a size distribution of the particles, following either a log-normal or normal distribution (with no negative radii allowed). Each simulation was performed three times, allowing to compute a mean and standard deviation of each data point. To validate our simulations, a series of tests were conducted. The magnetization of a mono-disperse, non interacting simulated sample with a null anisotropy constant K was compared to the Langevin theory (see fig. S2); the dependence of the magnetization on the cut-off radius of the dipolar interaction was studied, revealing a convergence of the magnetization for a R_C higher than 5 times the mean distance between particles (see fig. S1); and the simulations with anisotropy compared quantitatively with theoretical results obtained by Respaud [21] (see fig. S3). The simulation parameters were also optimized, i.e. it was checked that the magnetization value had properly converged for the parameter values inputted in the algorithm. The simulations presented in this work were conducted with 5000 nanoparticles, 250000 equilibration steps and 10^6 total simulation steps. As opposed to previous studies on the topic [43, 39, 44, 41, 45, 46, 47, 48], we choose the new magnetic moment and anisotropy axis at random and not within a solid angle around its previous direction. The underlying assumption is that our system is ergodic, because we are limiting our study to superparamagnetic states. The average acceptance rate of the new magnetic moment in our algorithm ranged from 11% for the 6nm radius

particles with all energy constraints considered to 42% for the 3nm radius particles with only the Zeeman interaction considered in the hamiltonian. That range is close to the approximate ideal acceptance rate of 23% for a Metropolis algorithm in high dimensions [49]. The acceptance rate of the new anisotropy axis was higher, ranging from 47% to 94% for simulations in which it was relevant. For detail, see supplementary material. The simulation code was written in C++ using the Boost library and the GNU Scientific Library (GSL).

2.2 Experiments

3nm iron oxide particles suspended in toluene and coated with a layer of oleic acid were purchased from HiQ Nano. Scanning transmission electron microscopy (STEM) images of the samples were obtained on a Tecnai Osiris Microscope, using a 200kV voltage and 0.057nA beam current. One of them is presented on figure 1. The presence of a $1-2$nm layer of oleic acid can be inferred from that image: it can be seen that the magnetic cores are not in contact, even though STEM images are obtained with dried samples. From that STEM image, using ImageJ, the diameter of 345 particles was measured. Their distribution was then fitted to a log-normal distribution. The particles presented a fairly narrow log-normal size distribution, with a median

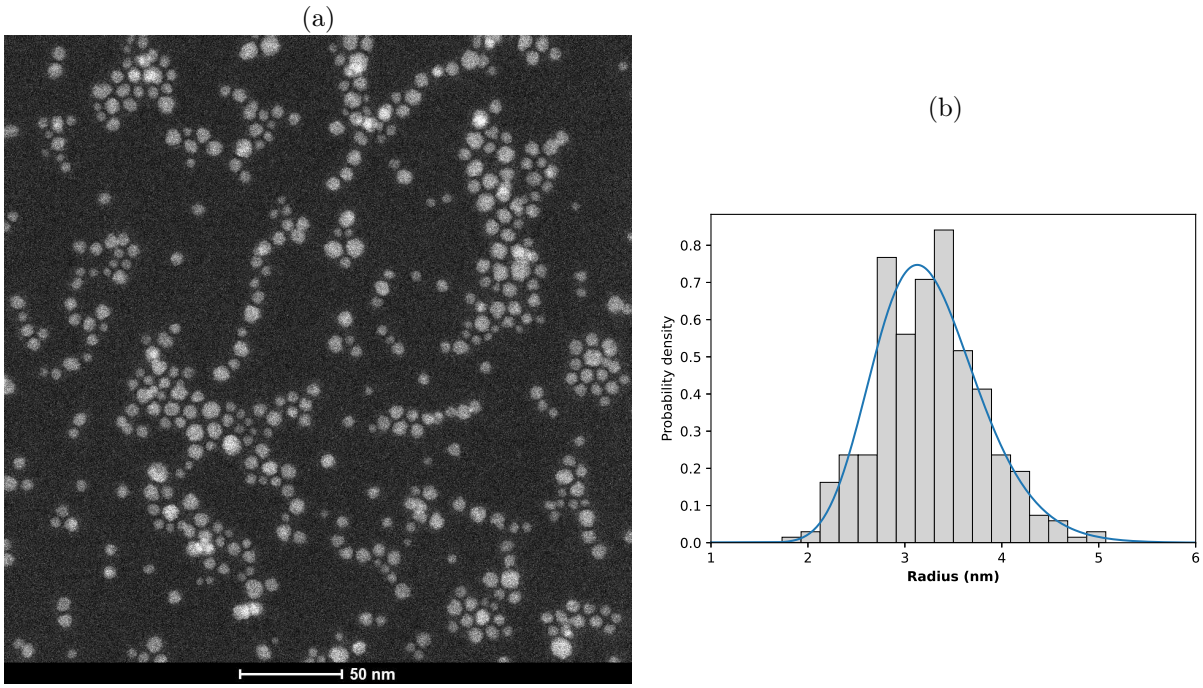

Figure 1: (a) STEM image of HiQ Nano particles with a 3nm median radius. (b) Radius distribution histogram of 345 particles visible on the STEM images.

radius R_0 of 3.21nm and σ_L-parameter 0.16. This is consistent with the manufacturer's announced median radius of 3nm. Dynamic Light Scattering (DLS) measurements of the sample were performed on a Malvern Zetasizer (see figure S4). The mean hydrodynamic radius is 5.77nm. Considering that the magnetic cores have a median radius of 3.21nm as determined by STEM, and are coated with a $1-2$nm layer of oleic acid, it can be assumed that the suspension is constituted of isolated homogeneously distributed particles without clustering. The iron concentration of the sample was measured through Atomic Emission Spectroscopy after microwave-assisted acidic digestion, yielding $[Fe] = 19.8$mg/mL. This is consistent with the manufacturer's nominal concentration of 20mg/mL. All samples were initially prepared with 50µL of the concentrated solution, and the solid samples were then obtained by letting the solvent evaporate. Some of these samples were dried under a 0.5T magnetic field, either parallel to the external field B_0 or perpendicular to it. The magnetic measurements were conducted on a Mini High Field System (Cryogenics) using the Vibrating Sample Magnetometer option. The diamagnetic contribution of the sample carrier and the solvent to the signal was removed by linearly fitting ($\mu_{tot}(B) = m \cdot B + p$) the two high-field regions of the curve, where

superparamagnetism does not contribute anymore to signal variations, averaging the parameters m and p obtained from those two fits, and then removing from the signal at each field the diamagnetic contribution computed from the average values of the parameters:

$$\mu_{corr}(B) = \mu_{raw}(B) - (\langle m \rangle B + \langle p \rangle) \tag{13}$$

Then, the signal (in electromagnetic units) was converted to A/m, through the formula :

$$M(\text{A/m}) = \frac{M(\text{emu}) \cdot f_{M,Fe} \cdot \rho_{mag}}{50 \cdot 10^{-6} \cdot C \cdot 10^{-3}} \tag{14}$$

where :

- M(A/m) is the magnetization in A/m;
- $M(e\text{emu})$ is the raw magnetic moment in electromagnetic units;
- $50 \cdot 10^{-6}$L is the sample volume;
- $f_{M,Fe}$ is the mass fraction of iron in either magnetite (0.72) or maghemite (0.699), depending on which iron oxide the sample is assumed to be. Unless specified otherwise, samples were always assumed to be pure magnetite in this article ;
- ρ_{mag} is the density in g/cm^3 of either magnetite ($\rho_{mag} = 5.17$g/cm^3) or maghemite ($\rho_{mag} = 4.9$g/cm^3 [50]) depending on which iron oxide the sample is assumed to be.

In most experimental samples, the particles are assumed to be a mix of magnetite and maghemite.

2.3 Fits

As mentioned previously, the integrated Langevin equation (5) is often used to fit the magnetization curves of experimental samples, and one goal of this research is to probe how accurate the size distributions obtained through that fit are. To perform the fits, we used the *curve_fit* routine from the *optimize* package of the SciPy library, with the mean radius $\langle R \rangle$, the standard deviation σ_N and the saturation magnetization M_S as fit parameters in the case of normal distributions, and the median radius R_0, σ_L parameter and saturation magnetization M_S in the case of log-normal distributions. The fits were performed on full magnetization curves, from -5T to 5T. The integration intervals were adapted to the size distribution parameters: for normal distributions the integration was performed from $R_0 - 4\sigma_N$ to $R_0 + 4\sigma_N$, and for log-normal distributions from $R_0 e^{-4\sigma_L}$ to $R_0 e^{4\sigma_L}$, as those intervals contained 99.99% of the distribution. The errors on the fit parameters were computed as the square roots of the diagonal elements of the covariance matrix, which were provided by the routine.

3 Results

3.1 Effect of the sole size distribution

In this section, the sole effect of the size distribution is probed. The simulated particles therefore exhibit no magnetic anisotropy, and are non-interacting. Figure 2 presents the magnetization curves of simulated samples with varying size dispersions, in the case of a lognormal and of a normal size distribution. In both cases, the broader the distribution, the faster the saturation of the magnetization. The curves were fitted using the integrated Langevin equation (5), yielding the parameters listed in table 1. They are very close to the input size distribution parameters, which validates the fitting program. For the rest of this paper, only log-normal distributions were considered, as the particle radii in the experimental sample follow a log-normal.

3.2 Effect of the anisotropy

Next, the effect of particle anisotropy on the curves was probed. In this subsection, the simulated particles do not interact. However, as magnetic anisotropy is considered, rotation can have an influence on the curves. For each graph and table, the state of the sample (dried, i.e. with rotation of the particles inhibited, or liquid, i.e. with rotation of the particles allowed) is specified.

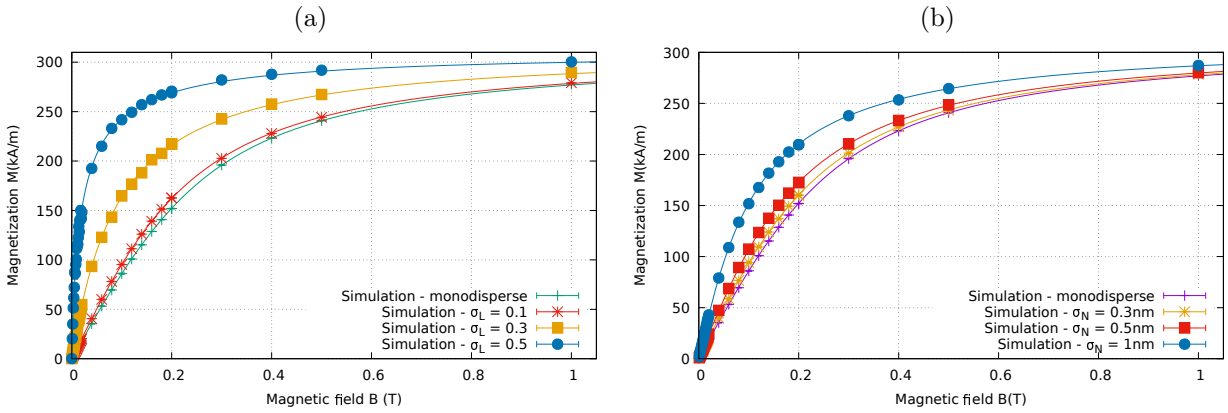

Figure 2: Simulated magnetization curves of samples of nanoparticles with various size distributions (no dipolar interaction, no anisotropy) at 300K (a) with a log-normal distribution of their radii - $R_0 = 3$nm (b) with a normal distribution of their radii - $\langle R \rangle = 3$nm.

Dist. type	**Input**			**Fitted parameters**		
Log-normal	R_0 (nm)	σ_L	M_S (kA/m)	R_0 (nm)	σ_L	M_S (kA/m)
	3	0.1	314.3	3.0265 ± 0.0039	0.0923 ± 0.0019	312.87 ± 0.09
		0.3		3.050 ± 0.012	0.2947 ± 0.0019	311.72 ± 0.24
		0.5		3.15 ± 0.07	0.491 ± 0.007	310.2 ± 0.6
Normal	R_0 (nm)	σ_N (nm)	M_S (kA/m)	R_0 (nm)	σ_N (nm)	M_S (kA/m)
	3	0.3	314.3	3.0241 ± 0.0035	0.275 ± 0.006	312.92 ± 0.09
		0.5		3.0380 ± 0.0047	0.4746 ± 0.0049	312.60 ± 0.10
		1		3.097 ± 0.012	0.965 ± 0.007	311.61 ± 0.15

Table 1: Distribution parameters obtained by fitting the simulated magnetization curves at 300K (no dipolar interaction, no anisotropy, see fig. 2) to the integrated Langevin equation, for six simulations with varying size distributions.

3.2.1 Effect of the rotation on the curves

To evaluate if differences between the magnetization curves of solid and liquid samples are caused by Brown relaxation, the influence of the rotation (i.e. of the Brown relaxation process, or in a more physical manner, the solid or liquid state of the sample) on the curves of anisotropic particles was first probed. To that effect, simulations were performed twice, once with the standard code, and once with rotation explicitly blocked in the algorithm. The resulting curves are presented on figure 3. The simulations with and without rotation (random anisotropy axes) overlap for $\sigma_L = 0.1$ and $\sigma_L = 0.3$, which indicates that there is no effect of the rotation on the magnetization curves of non-interacting particles with a median radius of 3nm, a narrow size distribution, and (initially) distributed anisotropy axes at 300K. For the broadest size distribution ($\sigma_L = 0.5$), a slight difference between the curves with and without rotation can be seen, hence Brown relaxation does impact the magnetization curve. The size distribution parameters obtained from fitting those curves are presented in table 2. The values are close for the liquid and solid samples, except for high dispersion parameters σ_L.

3.2.2 Effect of the easy axes' alignment on the curves

Next, the effect of the easy axes' alignment on the curves was probed. Brown relaxation was explicitly blocked in all cases to model the drying of the sample which was performed in the experiments (which will be presented further). The resulting curves can be seen on figure 4. Two different cases were considered: anisotropy axes parallel to the external field (which is along the Oz axis), and axes perpendicular to the

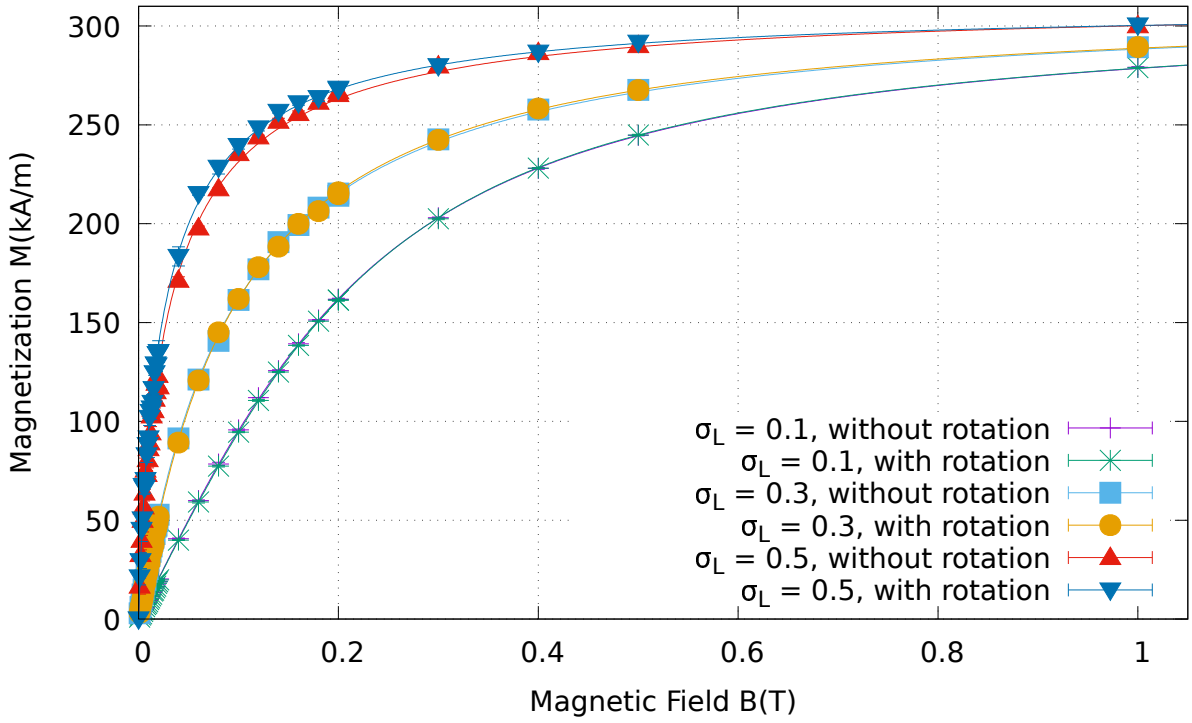

Figure 3: Comparison of the simulated magnetization curves of samples of nanoparticles with various size distributions (no dipolar interaction) at 300K with and without allowing the particles to rotate. Anisotropy axes are randomly oriented in the sample. $K = 13600\text{J/m}^3$. f = 0.005.

external field (specifically, aligned with the Oy axis). As a reference, the simulations with (blocked) randomly distributed anisotropy axes are plotted in a dashed line. In all cases, K = 13600 J/m^3. For each situation, three dispersion parameters σ_L were considered. It should be noted that the fit curve for $\sigma_L = 0.5$ in the case of anisotropy axes aligned to Oy (i.e. axes perpendicular to the external field) is not satisfactory. As can be seen on figure 4, there is a clear impact of the orientation of the easy axes on the magnetization curves of non-interacting nanoparticles with a median radius of 3nm. When the anisotropy axes are parallel to the external field, the saturation is faster. On the other hand, when the axes are perpendicular to the external field, the saturation is slower. The size distribution parameters and saturation magnetizations obtained from fitting those curves, compared with the parameters obtained by fitting the simulations with (randomly) distributed anisotropy axes, are presented in table 3. The size dispersion parameters obtained from fitting the curves with anisotropy axes parallel to the external field are significantly (10 to 55 %) higher than the parameters obtained from fitting the curves with randomly distributed anisotropy axes. On the other hand, the size dispersion parameters obtained from fitting the curves with anisotropy axes perpendicular to the field axis are significantly lower (9 to 31 %) than the parameters obtained from fitting the curves with randomly distributed anisotropy axes. The fit of the simulation with axes perpendicular to the field and the highest σ_L parameter was not considered in these percentages, because it has a 100% error.

3.3 Effect of the dipolar interaction

3.3.1 For particles without a size dispersion

To isolate the sole effect of the dipolar interaction, the simulated particles first had no magnetic anisotropy, and all had a median radius of 3 nm. As can be seen on figure 5a, there is no effect of the dipolar interaction between particles, within "error" (i.e. the standard deviation of the computations), on the magnetization at 300K, nor at 50K (see fig. S5(a)). Only at 10K for f = 0.1 (see fig. S5(b)) is an influence notable, but this simulation result should be interpreted with caution. In a real system, the particles are no longer superpara-

Sample state	Input			Fitted parameters		
	R_0 (nm)	σ_L	M_S (kA/m)	R_0 (nm)	σ_L	M_S (kA/m)
Liquid (Rotation allowed)	3	0.1	314.3	3.0444 ± 0.0047	0.0781 ± 0.0026	312.87 ± 0.09
		0.3		3.062 ± 0.012	0.2890 ± 0.0018	311.7 ± 0.23
		0.5		3.53 ± 0.07	0.426 ± 0.007	310.1 ± 0.7
Solid (Rotation inhibited)	3	0.1	314.3	3.0244 ± 0.0041	0.0929 ± 0.0020	312.92 ± 0.10
		0.3		3.157 ± 0.012	0.2714 ± 0.0020	311.24 ± 0.23
		0.5		3.32 ± 0.09	0.427 ± 0.009	311.8 ± 1.0

Table 2: Distribution parameters obtained by fitting the simulated magnetization curves at 300K to the integrated Langevin equation, for six simulations with varying size distributions. Anisotropy is considered, but dipolar interaction between the magnetic cores is not.

Sample state	Input			Fitted parameters		
	R_0 (nm)	σ_L	M_S (kA/m)	R_0 (nm)	σ_L	M_S (kA/m)
Solid (axes randomly distributed)	3	0.1	314.3	3.0244 ± 0.0041	0.0929 ± 0.0020	312.92 ± 0.10
		0.3		3.062 ± 0.012	0.2890 ± 0.0018	311.70 ± 0.23
		0.5		3.32 ± 0.09	0.427 ± 0.009	311.8 ± 1.0
Solid (axes $\parallel$)	3	0.1	314.3	3.1309 ± 0.0038	0.1023 ± 0.0016	311.93 ± 0.09
		0.3		2.830 ± 0.018	0.3787 ± 0.0024	311.75 ± 0.32
		0.5		2.30 ± 0.09	0.663 ± 0.010	309.2 ± 0.7
Solid (axes $\perp$)	3	0.1	314.3	2.9769 ± 0.0041	0.0841 ± 0.0022	313.40 ± 0.10
		0.3		3.331 ± 0.011	0.1991 ± 0.0024	310.76 ± 0.22
		0.5		4.759 ± 0.017	0.0 ± 0.7	310.4 ± 0.7

Table 3: Distribution parameters obtained by fitting the simulated magnetization curves at 300K to the integrated Langevin equation, for six simulations of solid samples with varying size distributions and orientations of the easy axes. No dipolar interaction between the magnetic cores was considered.

magnetic at this temperature, because most of the particles are blocked. As a consequence, no equilibrium state can be reached, whereas our simulations only consider equilibrium states. It is worth noting that no impact of the dipolar interaction can be observed even with very high volumic fractions of nanoparticles ($f > 0.1$, which would correspond to concentrations over 370mg/mL for magnetite nanoparticles, and over 470mg/mL for maghemite nanoparticles). At 300K (figure 5b), simulations in which the particles were positioned in contact with each other on a cubic grid network, leading to an extremely high volumic fraction of 0.46, were also performed. They confirm the results obtained at $f = 0.1$: a negligible impact of the dipolar interaction alone, within statistical variation, on M(B) curves. An effect of dipolar interaction can however be observed at 300K for larger particles, with a radius $R = 7$nm, as can be seen on figure S6.

3.3.2 For particles with a size distribution, and magnetic anisotropy

Curves including both anisotropy, with distributed axes ($K = 13600\text{J/m}^3$), and dipolar interaction ($f = 0.1$) were also obtained, and can be seen on figure 6, for three different size dispersion parameters. Dipolar interaction has no effect on the curves for $\sigma_L = 0.1$ and $\sigma_L = 0.3$, and at first glance seemingly a slight effect on the curves for the highest dispersion parameter ($\sigma_L = 0.5$). However, at low fields, the curves ($\sigma_L = 0.5$) are clearly different, as can be seen on the inset of figure 6 which translates in a significant difference in the parameters obtained from fitting both curves.

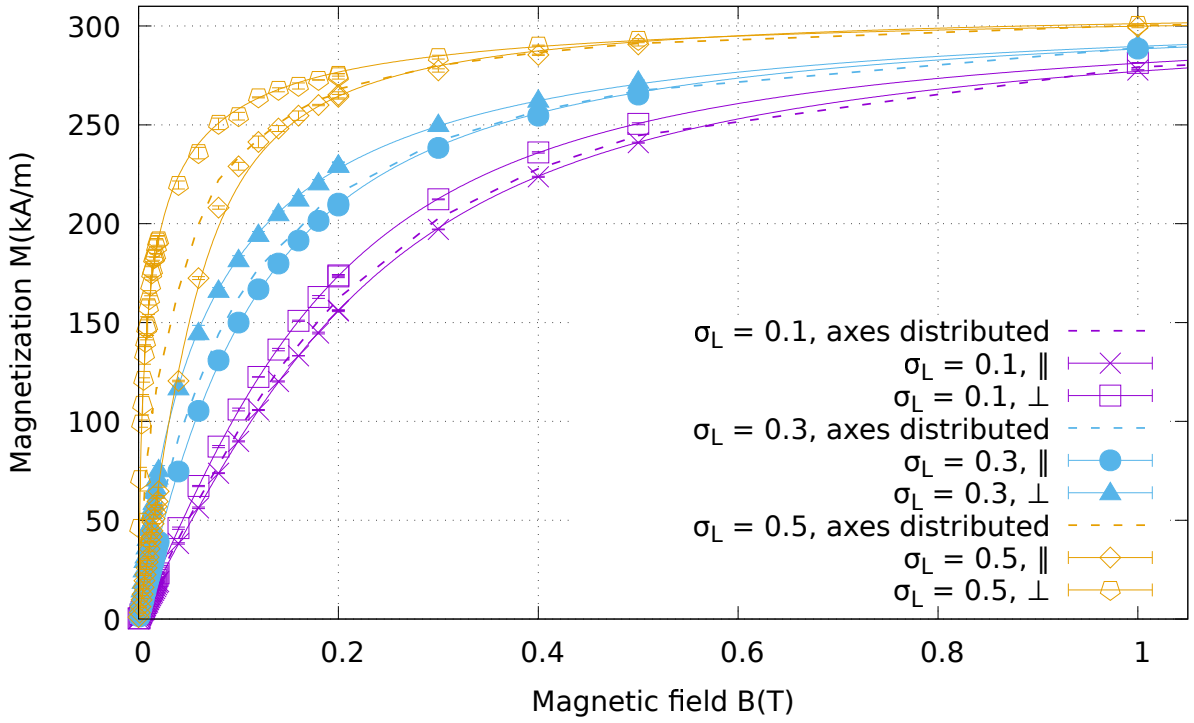

Figure 4: Simulated magnetization of particles exhibiting a log-normal size distribution, with a median radius of 3nm and varying σ_L-parameters, at 300K. Various orientations of their easy magnetization axes were considered, and were kept for the whole duration of the simulation so as to mimic a solid sample. The particles did not interact.

3.4 Experimental results

The magnetization curves of three dried samples were obtained, at 300K. The three samples were prepared from the same batch of HiQ Nano particles (hence, they had the same particle size distribution, concentration, and magnetic anisotropy constant), but they differed in their drying conditions. One was dried under a 0.5T magnetic field parallel to the experimental measurement field, one under a 0.5T magnetic field perpendicular to the experimental field, and one was dried in the absence of a magnetic field. The saturation magnetization used in all the simulations presented henceforth was not fitted from the curves, but was taken as the highest value of the magnetization of the sample at $\left|\vec{B}\right| = 5\text{T}$. As can be seen on figure 7, the drying method has a significant effect on the curves. Specifically, when the particles have been dried under a perpendicular magnetic field, the magnetization saturates at significantly higher fields than when they have been dried under zero field. On the other hand, when the particles have been dried under a parallel magnetic field, the magnetization saturates at significantly lower fields than when dried under no field. The dispersion parameter σ_L obtained by fit is also very dependent on the drying conditions of the sample, as can be seen in table 5, which presents the size distribution parameters fitted from the various curves. When the sample has been dried under a parallel field, the fitted σ_L is higher than that obtained by fitting the curve of a sample dried in the absence of a magnetic field (by 17%). On the other hand, when dried under a perpendicular field, the σ_L parameter is lower by 23% compared to the sample dried without a magnetic field.

3.5 Comparison between experimental and simulation results

Finally, the 300K magnetization curve of a solid sample was simulated using the size distribution and saturation magnetisation of the dried experimental sample, and compared to the experimental curve. Therefore, in these simulations, rotation was inhibited to better model the solid state of the sample, and a very high volumic fraction was used ($f = 0.27$). It should however be noted that the volume fraction does not influence the shape of the magnetisation curve in those conditions (fig. S7). Similar results can be obtained

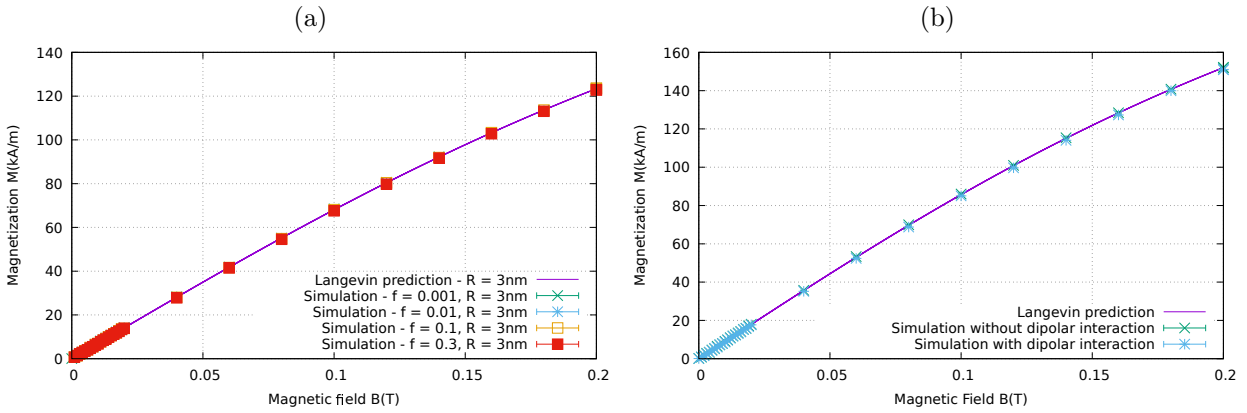

Figure 5: Simulated magnetization curves of interacting nanoparticles with a 3nm radius at 300K, depending on the particle volumic fraction. (a) randomly placed (b) placed on a grid (f = 0.46)

Sample	**Input**			**Fitted parameters**		
	R_0 (nm)	σ_L	M_S (kA/m)	R_0 (nm)	σ_L	M_S (kA/m)
Non-interacting	3	0.1	314.3	3.0244 ± 0.0041	0.0929 ± 0.0020	312.92 ± 0.10
		0.3		3.062 ± 0.012	0.2890 ± 0.0018	311.70 ± 0.23
		0.5		3.32 ± 0.09	0.427 ± 0.009	311.8 ± 1.0
Interacting	3	0.1	314.3	3.0147 ± 0.0040	0.0964 ± 0.0018	312.97 ± 0.09
		0.3		3.063 ± 0.012	0.2869 ± 0.0019	311.81 ± 0.23
		0.5		4.141 ± 0.038	0.2997 ± 0.0042	309.47 ± 0.48

Table 4: Size distribution parameters obtained by fitting the magnetization curve of six simulations with varying size distributions to the integrated Langevin equation. The simulations with interacting nanoparticles ($f = 0.1$), are compared to their equivalent with non-interacting particles. The particles had magnetic anisotropy, with randomly distributed and fixed easy axes so as to mimic a solid sample dried under zero field. The curves are presented in figure 6.

for the liquid sample, since as previously shown, free rotation of the particles does not impact the curves. The saturation magnetization input in the simulations was the highest value of the magnetization at 5T of the experimental sample, after correcting for diamagnetism. Because this value depends on how the total magnetic moment (in electromagnetic units) is converted to the total magnetization (in A/m), it depends on whether the sample is assumed to be magnetite or maghemite. The maghemite/magnetite proportion of the sample could be determined via Mossbauer spectroscopy [51]. However, this proportion can evolve over time through oxidation [52]. Therefore, two extreme cases were considered here: pure magnetite (figure 8(a)) and pure maghemite (figure 8(b)). The size distribution was here directly input from the TEM; the radii of the 345 particles who were measured were directly introduced into the algorithm. 15 copies of each particle were made so as to obtain enough particles to ensure proper convergence of the magnetization. The agreement between simulation and experiment is very good, especially if the sample is assumed to be maghemite. Curves with two other ways of inputting the size distribution into the algorithm were also produced:

- the size distribution histogram was fitted to a lognormal, yielding a median radius $R_0 = 3.21$nm and dispersion parameter $\sigma_L = 0.16$. 5000 radii were then sampled from that distribution, and directly input in the code.
- the size distribution histogram was fitted to two normal peaks, and 5000 radii were sampled from the superposition of those two peaks, and directly input in the code.

Predictably, the three curves using the three different evaluations of the size distribution superimpose (see fig. S8).

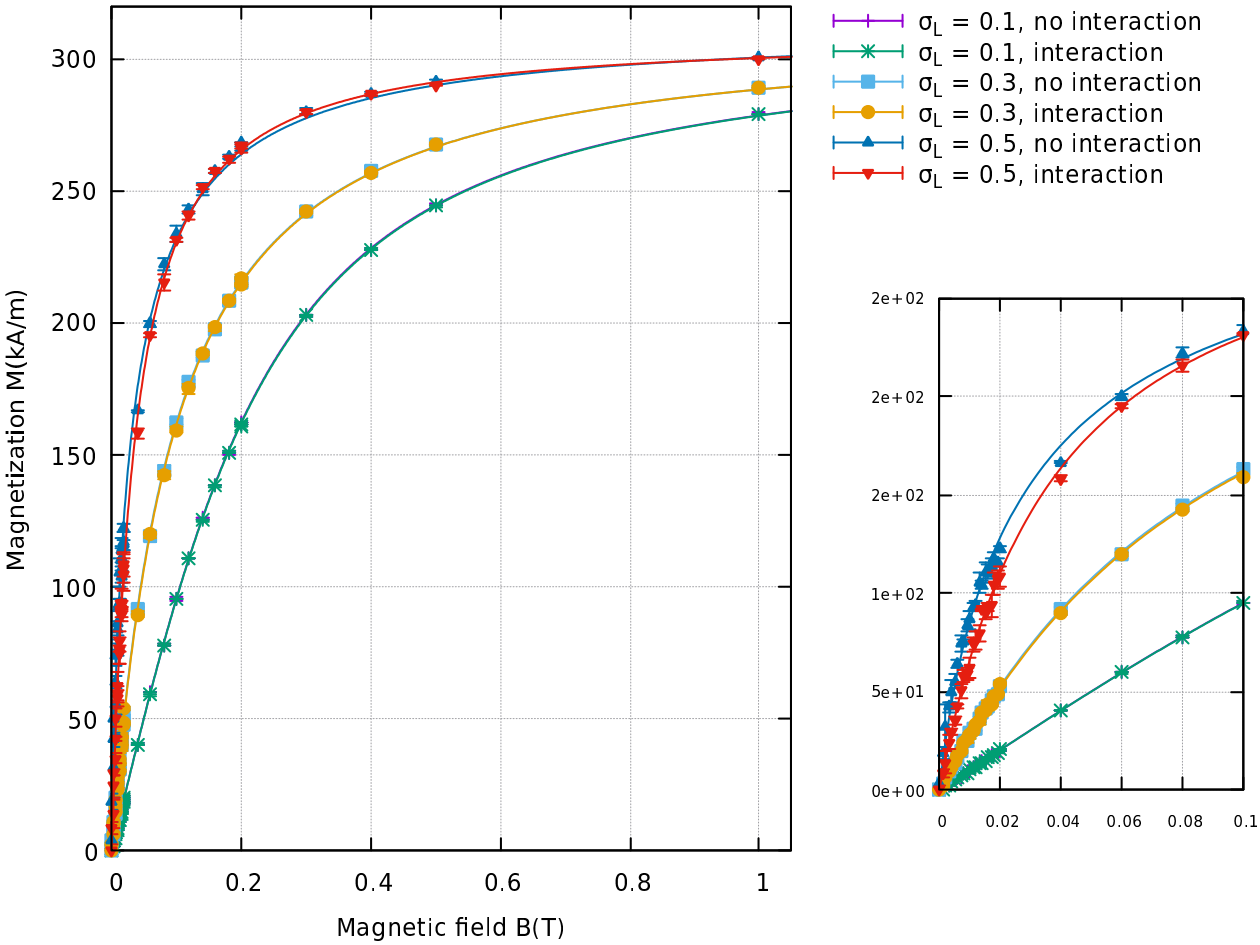

Figure 6: Simulated magnetization curves of dried interacting nanoparticles ($f = 0.1$) with a 3nm radius at 300K, with varying size distributions. The particles exhibit magnetic anisotropy ($K = 13600\text{J/m}^3$). The size distribution parameters obtained from fitting those curves can be found in table 4. On the right a zoom on low field values is presented.

Sample	**Oxide considered**	**Median radius** (nm)	σ_L	**Saturation magnetization** (kA/m)
Liquid	Magnetite	3.067 ± 0.016	0.1534 ± 0.005	355.636
	Maghemite	3.152 ± 0.017	0.153 ± 0.005	327.420
Dried without field	Magnetite	3.043 ± 0.016	0.1673 ± 0.004	348.111
	Maghemite	3.128 ± 0.016	0.1673 ± 0.0048	320.492
Dried under a 0.5 T $\parallel$ field	Magnetite	3.049 ± 0.017	0.1955 ± 0.0044	348.747
	Maghemite	3.134 ± 0.018	0.1956 ± 0.0044	321.077
Dried under a 0.5T $\perp$ field	Magnetite	3.076 ± 0.017	0.128 ± 0.006	345.889
	Maghemite	3.162 ± 0.018	0.128 ± 0.006	318.446

Table 5: Size distribution parameters obtained by fitting the magnetization curve of three solid samples and one liquid sample of HiQ Nano particles with a median radius of 3.21nm and a dispersion parameter $\sigma_L = 0.16$ to the integrated Langevin equation. The curves are presented in figure 7. The saturation magnetization was fixed and set to the highest value of the 5T magnetization of the sample.

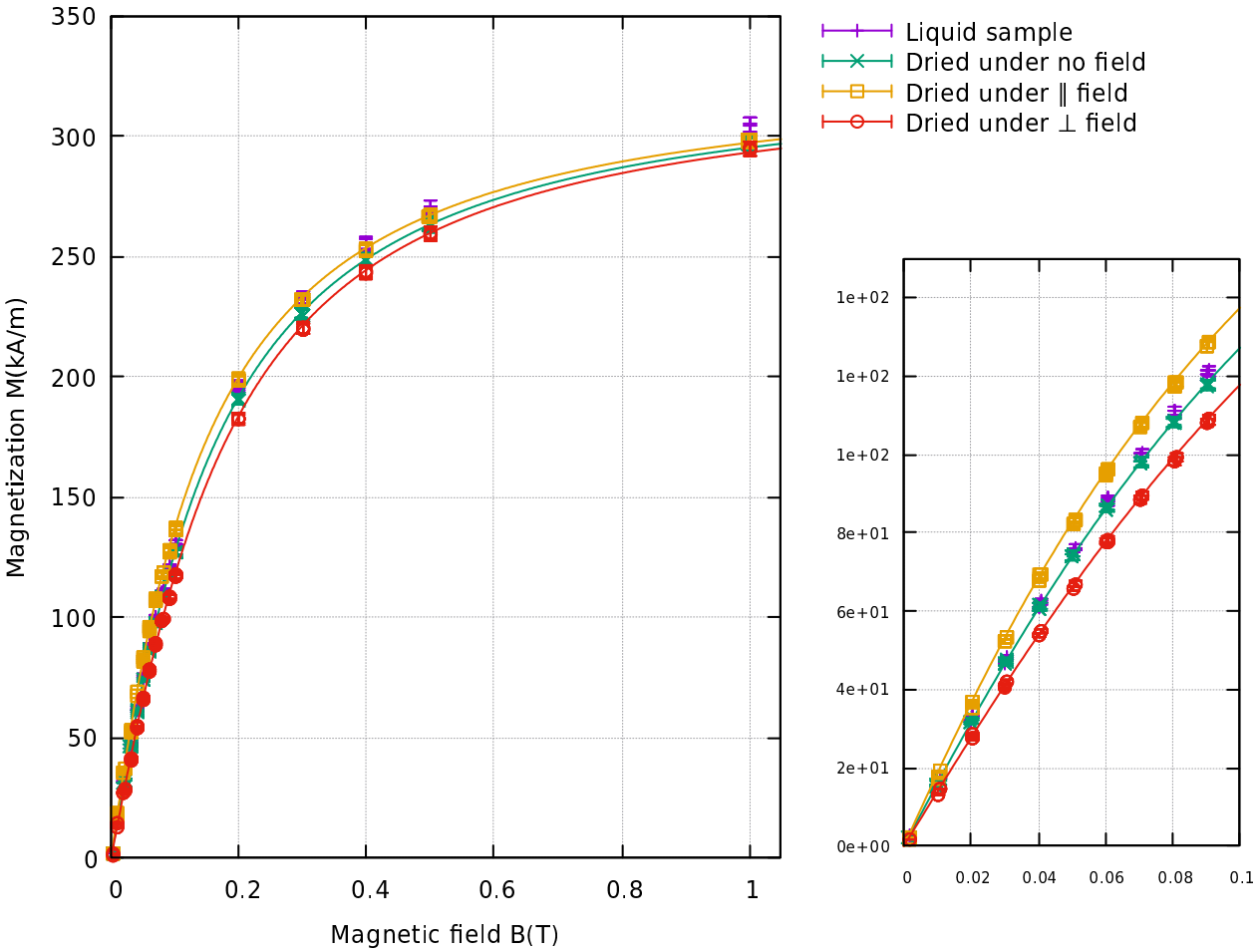

Figure 7: Experimental magnetization curves of three solid samples of HiQ Nano nanoparticles with a median radius of 3nm, dried under different magnetic conditions, at 300K, compared with the magnetization curve of the liquid sample. The size distribution parameters obtained from fitting those curves can be found in table 5. On the right a zoom on low field values is presented.

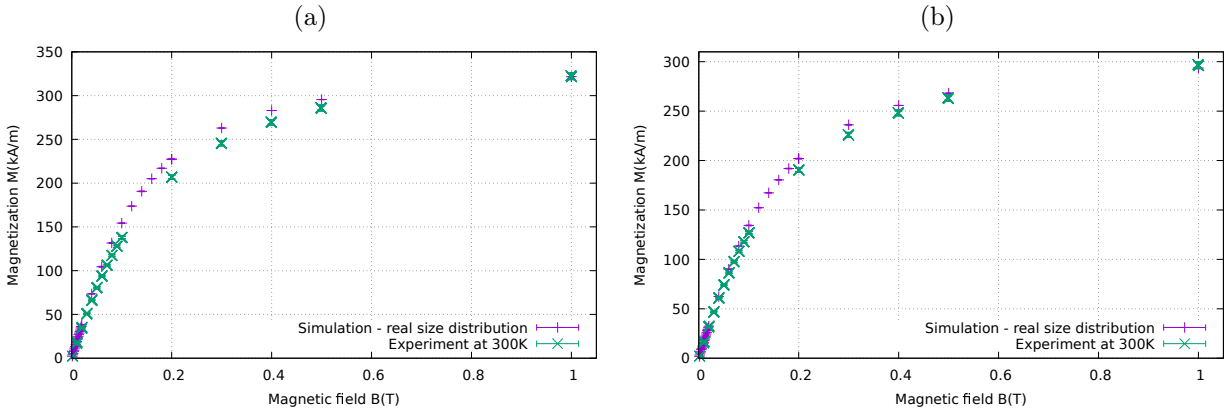

Figure 8: Experimental magnetization curve of the dried experimental sample, compared with the simulation performed with the size distribution from the TEM measurement. In the simulation, dipolar interaction between particles was considered ($f = 0.27$), and particle anisotropy was considered ($K = 13600\mathrm{J/m^3}$ and the axes are randomly distributed). Saturation magnetization was the highest value of the experimental 5T magnetization. Conversion of the magnetization from emu to amperes per meter was performed by assuming the particles were (a) pure magnetite, versus (b) pure maghemite.

4 Discussion

As previously noted [33], the Langevin fitting method is not accurate at 300K for particles with radii above $\sim$ 11nm, because those particles are no longer superparamagnetic. Our results indicate that even for superparamagnetic particles, the various effects that are not taken into account in Langevin theory, even when accounting for size distribution, cause significant deviations from the magnetization it predicts. Fitting the magnetization curves with equation (5) to obtain the size distribution parameters from a sample is therefore not always an accurate method.

4.1 Impact of the size distribution

On its own, the dispersion of sizes in the sample leads to a faster saturation than the theory predicts. The size distribution broadness can be gauged by the σ_L and σ_N parameters. The broader the size distribution, the faster the saturation of the magnetization for both normal and lognormal distributions. This is a well-known result [28, 39] which validates the simulations. As mentioned previously, the size distribution can be accounted for by integrating the Langevin equation. Fitting the simulations to integrated equation (5) yields fairly correct size parameters, as can be seen in table 1. This fit therefore yields a good evaluation of the size distribution of non-interacting samples without magnetic anisotropy, at all temperatures (see fig. S9 and table S2 for an example at 150K). However, particles from experimental samples do exhibit anisotropy, and do interact. It is therefore useful to evaluate how the fit holds when taking into account those realities.

4.2 Impact of the magnetic anisotropy

Indeed, the particle anisotropy impacts the simulated magnetization curves, and therefore the size distribution parameters obtained by fitting them. It is interesting to note first that rotation (i.e. the liquid or solid state of the sample) does not influence the magnetization curves of small non-interacting particles with randomly distributed anisotropy axes, as can be seen on figure 3. It does have a visible influence when the size distribution is broad ($\sigma_L = 0.5$), and that influence can be explained by the bigger particles in the sample. Indeed, such a broad distribution contains about 4.5% particles with a radius greater than 7nm, and such particles have a significantly greater magnetic moment, which creates a strong incentive for them to realign their easy magnetization axes with the field, which is possible in a liquid solvent. Supplementary figure S10 shows that for monodisperse particles with a radius of 7nm, the curves with and without rotation are clearly different: with rotation the saturation is logically faster. This translates in different effective radii when fitting the curves to a simple langevin: the fitting of the liquid curve yields $R = (6.885 \pm 0.010)$nm and $M_S = (312.14 \pm 0.31)$kA/m, whereas the fitting of the solid curve yields $R = (6.833 \pm 0.023)$nm and $M_S = (308.7 \pm 0.7)$kA/m with a fit that is less satisfactory (see fig. S10). For polydisperse solid samples, the underestimation of the radius of the bigger particles then results in erroneous fit parameters.

For solid samples, the magnetization curve of a sample with randomly distributed anisotropy axes (as the curves of figure 3), which would correspond to a sample dried without a magnetic field, coincides within standard deviation to the magnetization curve of particles without anisotropy (as the curves in figure 2) for $\sigma_L = 0.1$ and 0.3, and differ for $\sigma_L = 0.5$. This is more clearly seen on supplementary figure S11, in which they are plotted together. For low dispersion parameters, it seems that the various competing tendencies of the distributed axes "even out", resulting in a magnetization similar to a model without anisotropy. For $\sigma_L = 0.5$, this symmetry disappears because of the significant fraction of big particles, which also affect the signal more. M. Respaud [21], in a previous theoretical description, evidenced an influence of magnetic anisotropy on the magnetization curves even in the case of distributed anisotropy axes, for particles with an anisotropy energy $E_A = 3.45 \cdot 10^{-20} J$. In our simulations, for particles with a 3nm radius, $E_A = 1.54 \cdot 10^{-21}$J, but in the case of a broader size distribution (like in our $\sigma_L = 0.5$ case), the bigger particles (at the most, for that distribution, $R \sim 10$nm and therefore E_A reaches $5.7 \cdot 10^{-20}$) behave as Respaud predicted, which explains that the case of distributed axes, for $\sigma_L = 0.5$ then yields a curve different to the case without anisotropy. The size distribution parameters obtained from fitting the curves discussed above to the integrated Langevin equation (5) can be found in the top part of table 1 (for the case without anisotropy) and the bottom part of table 2 (for the case with distributed anisotropy axes in a solid sample). They only correspond within error for $\sigma_L = 0.1$, but remain close for $\sigma_L = 0.3$.

In simulations of solid samples, the orientation of the anisotropy axes also has a strong impact on the parameters obtained by fitting the curves, as can be seen on figure 4. When the anisotropy axes are aligned with the external field, the saturation occurs faster than when they are randomly distributed, and even more so than when they are perpendicular to the field. This result was expected: when the easy magnetization axes are aligned with the magnetic field, the Zeeman and anisotropy contributions to the particle's energy cooperate to push the magnetic moments of the SPIONs to align with the field, more so than the Zeeman interaction alone (in samples without anisotropy). On the other hand, when the easy magnetization axes are perpendicular to the magnetic field, the Zeeman and anisotropy contributions to the particle's energy are in competition, which hinders the alignment of the magnetic moments with the field. These variations in the simulated magnetization curves translate, in the case of samples with a size distribution, in a completely artificial variation of the resulting fitted parameters. Specifically, as can be seen in table 3, the fitted dispersion parameter is impacted by the axes' orientation: when parallel to the measurement field B_0, σ_L is overestimated by 10 % to 55%, and when perpendicular to the field, σ_L is underestimated by 9 % to 31%. It seems that the fit interprets the faster saturation here as a broader size distribution (which would also lead to a faster saturation), since it does not take into account the anisotropy, and conversely slower saturation as a narrower size distribution. The simulated impact of the alignment of the axes with respect to the field on the magnetization curves is consistent with tendencies observed by Londoño Navarro et al [19]. The current study pushes it a bit further by fitting the curves, which allows for a quantification of the effect. These effects observed in the simulations compare qualitatively well with our experimental results. It is obviously not possible to choose the orientation of the easy magnetization axes of a sample of nanoparticles in solution. It is however possible to orientate them using a magnetic field when still in liquid state, and then block them by inhibiting Brown relaxation, i.e. by either freezing or drying the sample. If the sample was dried under a parallel field, the easy magnetization axes were aligned with the magnetic field before being blocked, and the results can be compared to the simulations where the axes were parallel to the field. On the other hand, if the sample was dried under a perpendicular field, the axes were blocked in a direction perpendicular to the magnetic field, and the resulting curve can be compared to the simulation where the axes were perpendicular to the field.

The comparisons hold up; the simulations with axes aligned to the external field, presented on figure 4 (which yield the fitted size distribution parameters presented in table 3) lead to a faster saturation of the magnetization and a higher dispersion parameter σ_L, same as the experiments on samples dried under a parallel magnetic field, presented on figure 7 (and leading to the fitted size distribution parameters from table 5). On the other hand, the simulations with axes perpendicular to the field lead to a slower saturation of the magnetization, and a lower dispersion parameter σ_L, same as the experiments on a sample dried under a perpendicular magnetic field. The relative impact of the easy axes being aligned with the field on the fitted σ_L parameter in the experiments is comparable to the relative impact observed in the simulations (σ_L is 17% higher when fitting the "parallel" curve, and 23% lower when fitting the "perpendicular" curve). The simulation and experimental results indicate that extra caution should be taken to dry (or freeze) samples under a controlled zero field. Indeed, the three samples presented here experimentally sport the same size distribution, since they come from the same batch of nanoparticles. The three simulations (for each size dispersion) also have the same, known, size distribution. However, the curves corresponding to drying in different conditions show different magnetization curves. Therefore, when fitted to the integrated equation, they yield different distribution parameters, which do not accurately reflect the actual size distribution of the samples if dried under a nonzero magnetic field.

4.3 Impact of the dipolar interaction between particles

Aside from anisotropy, the magnetic behaviour of solid samples is expected to be driven by the effect of dipolar interaction, as drying leads to volumic fractions of nanoparticles dramatically higher than those reached in solutions. To test that hypothesis, the effect of sole dipolar interactions on particles with no magnetocrystalline anisotropy, and without any size dispersion, was first probed. As can be seen on figure 5, there is no effect of dipolar interactions on the simulated magnetization curves of nanoparticles with a 3nm radius at 300K within error. This is consistent with previous simulation studies on the topic, although those focused on clusters of nanoparticles [28, 19]. As a consequence, the presence of dipolar interaction in the simulations does not modify the fitted parameters. Only at *both* low temperatures ($T \sim 10$K) and

high volume fractions ($f \sim 0.1$) do dipolar interactions impact the curves of such particles by lowering the magnetization (see fig. S5). Such volumic fractions correspond to a mean interparticle distance

$$\langle r_i j \rangle = \sqrt[3]{\frac{4\pi R^3}{3f}} \tag{15}$$

of 10nm for particles with a radius of 3nm. However, at low temperatures, the magnetic moments of the particles are blocked to Néel relaxation ($\tau_N > \tau_M$). As those processes are not taken into account in the simulations presented in this article, the magnetization curves obtained at those temperatures should not be taken as a realistic prediction of the behaviour of experimental samples; this is far beyond the scope of the simulations, which aim at modeling superparamagnetic systems. When a size dispersion of the particles and magnetic anisotropy are introduced in the simulation, an impact of dipolar interaction appears for broad distributions ($\sigma_L = 0.5$), as can be seen on figure 6 at 300K. This is again due to the bigger particles present in such a sample. As established before, in such a distribution, there are 4.5% of particles with a radius higher than 7nm, and for those bigger particles, the stronger dipolar interaction energy results in changes in the magnetization curve, even when they do not have magnetic anisotropy and all have the same size, as can be seen on supplementary figure S6. This also translates in significant variations in the parameters obtained by fitting the magnetization curves of interacting nanoparticles to the integrated Langevin equation (5): the dispersion parameter σ_L is dramatically underestimated, and the median radius R_0 is widely overestimated, both by 40%. Ivanov and Kuznetsova proposed a second-order modified mean-field model, which is an adapted Langevin theory accounting for interactions between particles. It reportedly yields consistent size distribution parameters over a wide range of concentrations, indicating that it performs well to evaluate size distributions of interacting samples [41]. However, it does not take into account magnetic anisotropy, which Monte Carlo simulations allow to do.

4.4 Comparison between the simulation and the experiments

Our simulations reproduce quite well the magnetization curve of a dried sample at 300K, as figure 8 shows. The discrepancies remaining between the simulation and the experiment have yet to be explained. One possible improvement of the simulations to be explored is refining the modeling of anisotropy, as the uniaxial model is rather simplistic; cubic anisotropy would be more realistic. As shown before, magnetocrystalline anisotropy can have a significant impact on magnetization curves, so a change in its definition could very well be the missing puzzle piece. The value of the anisotropy constant, within the typical range expected for magnetite, however has no influence on the simulated curves (see fig. S12), at this temperature and for randomly oriented axes (which is expected of a realistic sample). Another possibility are surface effects, which some authors consider in simulations or analytically (albeit without comparing to experimental results) [53]. Contrary to Schaller et al [28], the size distribution used in simulations to reproduce the experimental curve was evaluated from the TEM, independently from magnetic measurements. This makes the good agreement between simulation and experiments all the more interesting.

4.5 Limitations of our model

In this work, we chose to use a Metropolis-Hastings algorithm to model the behaviour of superparamagnetic iron oxide nanoparticles. It should be noted that this algorithm is built to study the equilibrium properties of systems. It is not suitable to study dynamical effects, such as the Néel and Brown relaxation processes. This limits the results that can be obtained by our methodology, in particular at low temperatures, because of the blocking of the magnetic moment of the particles. The absence of an effect of dipolar interactions on the magnetization curves of nanoparticles with a 3nm radius at 300K, even at high volumic fractions, could seem surprising. Indeed, dense clusters of iron oxide nanoparticles exhibit an important shift of the peak of their ZFC curves towards higher temperatures, when compared to the same, isolated particles [23, 54, 44]. This may be due to dipolar interaction modifying the Néel relaxation time [1] through the locally high fields it can produce. A previous theoretical study by Ilg and Kröger on the influence of dipolar interactions on the Néel and Brown relaxation times supports this hypothesis [55]. Such an effect of dipolar interactions on Néel time could explain how clustering affects field-cooling and zero-field-cooling magnetization curves [54] without affecting the magnetization curves at a given temperature.

5 Conclusion

In this article, the impact of different parameters influencing the magnetization curves of iron oxide nanoparticles was studied using Monte Carlo simulations. First, at 300K, drying a sample of nanoparticles with distributed anisotropy axes in the absence of a magnetic field does not modify the magnetization curves. Dipolar interaction has no influence on the curves either, even with high volumic fractions of the particles. Both those conclusions only hold as long as the particles are small, and exhibit a narrow size distribution: the presence of even few bigger particles sees the curves of the various simulated samples differ. Second, in solid samples, the orientation of the easy magnetization axes had a significant effect on the magnetization curves in both simulations and experiments. This highlights the importance of controlling the magnetic field under which samples are dried or frozen: it can have a significant impact on their magnetic properties. Special caution should be taken if the curves are to be fitted to an integrated Langevin equation to determine size distribution parameters, as the fitted dispersion parameter σ_L in particular is modified (by 9% to 55%) in samples dried under a magnetic field, whether parallel or perpendicular to the experimental field. The main finding of this paper is that overall, that fit has a very limited validity range; it only performs well for samples of non-interacting small particles with distributed anisotropy axes. Most experimental samples do not fit that bill, and therefore the size distribution parameters obtained by fitting experimental curves to the integrated Langevin equation should be used with caution. Finally, our simulations including all the known experimental parameters reproduce quantitatively well the magnetization curves of a liquid sample at 300K, which confirms the validity of the simulation model at such a temperature.

Highlights

- A method to simulate liquid and dry samples of superparamagnetic particles is built.
- The simulation results are compared whenever possible to experiments.
- Neither dipolar interaction nor particle rotation influence the curves at 300K.
- The orientation of the magnetocrystalline anisotropy axes does however.
- Deviations from Langevin behaviour cause Langevin fitting to behave poorly.

Funding Source

University of Mons (UMONS)

Acknowledgements

The authors thank Sophie Laurent from the university of Mons for the access to the Dynamic Light Scattering equipment.

Computational resources have been provided by the Consortium des Équipements de Calcul Intensif (CÉCI), funded by the Fonds de la Recherche Scientifique de Belgique (F.R.S.-FNRS) under Grant No. 2.5020.11 and by the Walloon Region.

Declaration of competing interest

The authors declare no competing interest.

Author contributions

Éléonore Martin: Methodology, Software, Validation, Investigation, Formal Analysis, Data Curation, Writing, Visualization

Sara Bals, Safiyye Kavak: TEM Imaging of the Experimental Sample

Yves Gossuin: Conceptualization, Methodology, Data Curation, Resources, Supervision

Quoc Lam Vuong: Conceptualization, Methodology, Software, Validation, Supervision

Data and code accessibility

All data, and the source code of the simulations and fits, are accessible upon request to the corresponding author.

References

[1] L. Néel, Theory of the magnetic after-effect in ferromagnetics in the form of small particles, with applications to baked clays, Gordon and Breach Science Publishers, 1988, Ch. A69, pp. 407–427.

[2] W. F. J. Brown, Thermal fluctuations of a single-domain particle, Physical Review 130 (5) (1963) 1677 – 1686. doi:10.1103/PhysRev.130.1677.

[3] Q. L. Vuong, P. Gillis, A. Roch, Y. Gossuin, Magnetic resonance relaxation induced by superparamagnetic particles used as contrast agents in magnetic resonance imaging: a theoretical review, WIREs Nanomedicine and Nanobiotechnology (4 2017). doi:10.1002/wnan.1468.

[4] A. S. Arbab, J. A. Frank, Cellular mri and its role in stem cell therapy, Regenerative Medicine 3 (2) (2008) 199–215. doi:10.2217/17460751.3.2.199.

[5] J. W. Bulte, In vivo mri cell tracking: Clinical studies, American Journal of Roentgenology 193 (2009) 314–325. doi:10.2214/AJR.09.3107.

[6] J. M. Hill, A. J. Dick, V. K. Raman, R. B. Thompson, Z.-X. Yu, K. A. Hinds, B. S. Pessanha, M. A. Guttman, T. R. Varney, B. J. Martin, C. E. Dunbar, E. R. McVeigh, R. J. Lederman, Serial cardiac magnetic resonance imaging of injected mesenchymal stem cells, Circulation 108 (2003) 1009–1014. doi:10.1161/01.CIR.0000084537.66419.7A.

[7] U. Himmelreich, T. Dresselaers, Cell labeling and tracking for experimental models using magnetic resonance imaging, Methods 48 (2009) 112–124. doi:10.1016/j.ymeth.2009.03.020.

[8] C. Hughes, J. Galea-Lauri, F. Farzaneh, D. Darling, Streptavidin paramagnetic particles provide a choice of three affinity-based capture and magnetic concentration strategies for retroviral vectors, Molecular Therapy 3 (4) (2001) 623–629. doi:10.1006/mthe.2001.0268.

[9] J. M. Perez, F. J. Simeone, Y. Saeki, L. Josephson, R. Weissleder, Viral-induced self-assembly of magnetic nanoparticles allows the detection of viral particles in biological media, Journal of the Americal Chemical Society 125 (2003) 10192–10193. doi:10.1021/ja036409g.

[10] E. A. Périgo, G. Hemery, O. Sandre, D. Ortega, E. Garaio, F. Plazaola, F. J. Teran, Fundamentals and advances in magnetic hyperthermia, Applied Physics Reviews 2 (4) (2015) 041302. doi:10.1063/1.4935688.

[11] M. Shahsavari Alavijeh, M. S. Bani, I. Rad, S. Hatamie, M. S. Zomorod, M. Haghpanahi, Antibacterial properties of ferrimagnetic and superparamagnetic nanoparticles: a comparative study, Journal of Mechanical Science and Technology 35 (2) (2021) 815–821. doi:10.1007/s12206-021-0143-x.

[12] B. Gleich, J. Weizenecker, Tomographic imaging using the nonlinear response of magnetic particles, Nature 435 (2005) 1214–1217. doi:10.1038/nature03808.

[13] J. Borgert, J. D. Schmidt, I. Schmale, J. Rahmer, C. Bontus, B. Gleich, B. David, R. Eckart, O. Woywode, J. Weizenecker, J. Schnorr, M. Taupitz, J. Haegele, F. M. Vogt, J. Barkhausen, Fundamentals and applications of magnetic particle imaging, Journal of Cardiovascular Computed Tomography 6 (15) (2012) 149–153. doi:10.1016/j.jcct.2012.04.007.

[14] F. Wiekhorst, U. Steinhoff, D. Eberbeck, L. Trahms, Magnetorelaxometry assisting biomedical applications of magnetic nanoparticles, Pharm Res 29 (2012) 1189–1202. doi:10.1007/s11095-011-0630-3.

[15] T. Neuberger, B. Schöpf, H. Hofmann, M. Hofmann, B. von Rechenberg, Superparamagnetic nanoparticles for biomedical applications: Possibilities and limitations of a new drug delivery system, Journal of Magnetism and Magnetic Materials 293 (2005) 483–496. doi:10.1016/j.jmmm.2005.01.064.

[16] J. Dunn, M. Fuller, J. Zoeger, J. Dobson, F. Heller, J. Hammann, E. Caine, B. M. Moskowitz, Magnetic material in the human hippocampus, Brain Research Bulletin 36 (2) (1995) 149–153. doi:10.1016/0361-9230(94)00182-z.

[17] P. Langevin, Sur la théorie du magnétisme, Journal de physique théorique et appliquée 4 (1) (1905) 678–693. doi:10.1051/jphystap:019050040067800.

[18] S. J. Kemp, R. M. Ferguson, A. P. Khandhar, K. M. Krishnan, Monodisperse magnetite nanoparticles with nearly ideal saturation magnetization, RSC Advances 6 (2016) 77452–77464. doi:10.1039/c6ra12072e.

[19] J. Londoño-Navarro, J. C. Riaño-Rojas, E. Restrepo-Parra, Competition between anisotropy and dipolar interaction in multicore nanoparticles: Monte carlo simulation, DYNA 82 (194) (2015) 66–71. doi:10.15446/dyna.v82n194.44297.

[20] F. Tournus, A. Tamion, Magnetic susceptibility curves of a nanoparticle assembly ii. simulation and-analysis of zfc/fc curves in the case of a magnetic anisotropy energy distribution, Journal of Magnetism and Magnetic Materials 323 (2011) 1118 – 1127. doi:10.1016/j.jmmm.2010.11.057.

[21] M. Respaud, Magnetization process of noninteracting ferromagnetic cobalt nanoparticles in the superparamagnetic regime: deviation from langevin law, Journal of Applied Physics 86 (1) (1999) 556–561. doi:10.1063/1.370765.

[22] H. Mamiya, H. Fukumoto, J. L. C. Huaman, K. Suzuki, H. Miyamura, J. Balachandran, Estimation of magnetic anisotropy of individual magnetite nanoparticles for magnetic hyperthermia, ACS Nano 14 (7) (2020) 8421–8432. doi:10.1021/acsnano.0c02521.

[23] C. E. Hoppe, F. Rivadulla, M. A. López-Quintela, M. C. Buján, J. Rivas, D. Serantes, D. Baldomir, Effect of submicrometer clustering on the magnetic properties of free-standing superparamagnetic nanocomposites, Journal of Physical Chemistry C 112 (34) (2008) 13099–13103. doi:10.1021/jp8039548.

[24] C. Plank, O. Zelphati, O. Mykhaylyk, Magnetically enhanced nucleic acid delivery. ten years of magnetofection - progress and prospects, Advanced Drug Delivery Reviews 63 (2011) 1300–1331. doi:10.1016/j.addr.2011.08.002.

[25] C. Wilhelm, F. Gazeau, Universal cell labelling with anionic magnetic nanoparticles, Biomaterials 29 (2008) 3161–3174. doi:10.1016/j.biomaterials.2008.04.016.

[26] R. Qiao, C. Yang, M. Gao, Superparamagnetic iron oxide nanoparticles: from preparations to in vivo mri applications, Journals of Materials Chemistry 19 (2009) 6274–6293. doi:10.1039/b902394a.

[27] O. Mykhaylyk, T. Sobisch, I. Almstätter, Y. Sanchez-Antequera, S. Brandt, M. Anton, M. Döblinger, D. Eberbeck, M. Settles, R. Braren, D. Lerche, C. Plank, Silica-iron oxide magnetic nanoparticles modified for gene delivery: A search for optimum and quantitative criteria, Pharmaceutical Research 29 (5) (2012) 1344–1365. doi:10.1007/s11095-011-0661-9.

[28] V. Schaller, G. Wahnström, A. Sanz-Velasco, P. Enoksson, C. Johansson, Monte carlo simulation of magnetic multi-core nanoparticles, Journal of Magnetism and Magnetic Materials 321 (2009) 1400–1403. doi:10.1016/j.jmmm.2009.02.047.

[29] M. Lévy, C. Wilhelm, M. Devaud, P. Levitz, F. Gazeau, How cellular processing of superparamagnetic nanoparticles affects their magnetic behavior and nmr relaxivity, Contrast Media and Molecular Imaging 7 (2012) 373–383. doi:10.1002/cmmi.504.

[30] M. Lévy, C. Wilhelm, N. Luciani, V. Deveaux, F. Gendron, A. Luciani, M. Devaud, F. Gazeau, Nanomagnetism reveals the intracellular clustering of iron oxide nanoparticles in the organism, Nanoscale 3 (2011) 4402–4410. doi:10.1039/c1nr10778j.

[31] M. Lévy, F. Gazeau, J.-C. Bacri, C. Wilhelm, M. Devaud, Modeling magnetic nanoparticle dipole-dipole interactions inside living cells, Physical Review B 84 (7) (2011) 075480–1 – 075480–11. doi:10.1103/PhysRevB.84.075480.

[32] D. Henrard, Q. L. Vuong, S. Delangre, X. Valentini, D. Nonclercq, M. F. Gonon, Y. Gossuin, Monitoring of superparamagnetic particle sizes in the langevin law regime, Journal of Nanomaterials 2019 (2019) 64092101–64092109. doi:10.1155/2019/6409210.

[33] R. Woodward, J. Heeris, T. St. Pierre, M. Saunders, E. Gilbert, M. Rutnakornpituk, Q. Zhang, S. Riffle, A comparison of methods for the measurement of the particle-size distribution of magnetic nanoparticles, Journal of Applied Crystallography 40 (2007) s495–s500. doi:10.1107/S002188980700091X.

[34] O. Petracic, Superparamagnetic nanoparticle ensembles, Superlattices and Microstructures 47 (2010) 569–578. doi:10.1016/j.spmi.2010.01.009.

[35] Viscosity of chloroform, "`https://wiki.anton-paar.com/en/chloroform/`", accessed: 2022-11-15.

[36] Viscosity of toluene, "`https://wiki.anton-paar.com/en/toluene/`", accessed: 2022-11-15.

[37] V. Rudyak, S. Krasnolutskii, Dependence of the viscosity of nanofluids on nanoparticle size and material, Physics Letters A 378 (26) (2014) 1845–1849. doi:https://doi.org/10.1016/j.physleta.2014.04.060.

[38] M. Shliomis, Effective viscosity of magnetic suspensions, Sov. Phys. JETP 34 (1972) 1291–1294.

[39] V. Russier, C. de Montferrand, Y. Lalatonne, L. Motte, Size and polydispersity effect on the magnetization of densely packed magnetic nanoparticles, Journal of applied physics 112 (7) (2012) 0739261–07392611. doi:10.1063/1.4757418.

[40] R. Chantrell, N. Walmsley, J. Gore, M. Maylin, Calculations of the susceptibility of interacting superparamagnetic particles, Physical Review B 63 (2) (2000) 0244101–02441014. doi:10.1103/PhysRevB.63.024410.

[41] A. O. Ivanov, S. S. Kantorovich, E. N. Reznikov, C. Holm, A. F. Pshenichnikov, A. V. Lebedev, A. Chremos, P. J. Camp, Magnetic properties of polydisperse ferrofluids: A critical comparison between experiment, theory, and computer simulation, Physical Review E 75 (2007) 061405. doi:10.1103/PhysRevE.75.061405.

[42] N. Metropolis, A. W. Rosenbluth, M. N. Rosenbluth, A. H. Teller, E. Teller, Equation of state calculations by fast computing machines, The Journal of Chemical Physics 21 (1953) 1087–1092. doi:10.1063/1.1699114.

[43] K. Trohidou, M. Vasilakaki, Monte Carlo Studies of Magnetic Nanoparticles, IntechOpen, New York, NY, 2011, Ch. 20, pp. 513–538.

[44] J. García-Otero, M. Porto, J. Rivas, A. Bunde, Influence of dipolar interaction on magnetic properties of ultrafine ferromagnetic particles, Physical Review Letters 84 (1) (2000) 167–170.

[45] D. Kechrakos, K. Trohidou, Magnetic properties of dipolar interacting single-domain particles, Physical Review B 58 (18) (1998) 12169–12178. doi:10.1103/PhysRevB.58.12169.

[46] L. Wang, J. Ding, H. Kong, Y. Li, Y. Feng, Monte carlo simulation of a cluster system with strong interaction and random anisotropy, Physical Review B 64 (2011) 214410. doi:10.1103/PhysRevB.64.214410.

[47] M. Zhongquan, D. Chen, Z. He, Equilibrium magnetic properties of dipolar interacting ferromagnetic nanoparticles, Journal of Magnetism and Magnetic Materials 320 (2008) 2335–2338. doi:10.1016/j.jmmm.2008.04.118.

[48] D. Dimitrov, G. Wysin, Magnetic properties of superparamagnetic particles by a monte carlo method, Physical Review B 54 (1996) 9237. doi:10.1103/PhysRevB.54.9237.

[49] A. Gelman, J. B. Carlin, H. S. Stern, D. B. Dunson, A. Vehtari, D. B. Rubin, Computationally efficient Markov chain simulation, 3rd Edition, CRC Press, 6000 Broken Sound Parkway NW, Suite 300, Boca Raton, FL 33487-2742, 2014, Ch. 12, pp. 293–310.

[50] I. Lucas, S. Durand-Vidal, E. Dubois, J. Chevalet, P. Turq, Surface charge density of maghemite nanoparticles: Role of electrostatics in the proton exchange, Journal of Physical Chemistry 111 (50) (2007) 18568–18576. doi:10.1021/jp074311.

[51] J. Fock, L. K. Bogart, D. González-Alonso, J. I. Espeso, M. F. Hansen, M. Varón, C. Frandsen, Q. A. Pankhurst, On the 'centre of gravity' method for measuring the composition of magnetite/maghemite mixtures, or the stoichiometry of magnetite-maghemite solid solutions, via 57fe mössbauer spectroscopy, Journal of Physics D: Applied Physics 50 (26) (2017) 265005. doi:10.1088/1361-6463/aa73fa.

[52] J.-M. Greneche, The contribution of ^{57}fe mössbauer spectrometry to investigate magnetic nanomaterials, in: Mössbauer Spectroscopy, 1st Edition, Springer, Berlin, Heidelberg, 2013, Ch. 4, pp. 204–205.

[53] F. Vernay, Z. Sabsabi, O. Iglesias, H. Kachkachi, Surface effects on the magnetic behavior of nanoparticle assemblies, Physical Review B 521 (2012) 012010. doi:10.1088/1742-6596/521/1/012010.

[54] N. Ortiz-Gordoy, D. G. Agredo-Diaz, A. O. Garzón-Posada, C. A. Parra Vargas, D. A. Landínez Téllez, J. Roa-Rojas, A facile method to produce magnetic nanoparticles and its influence on their magnetic and physical properties, Materials Letters 293 (2021) 129700. doi:10.1016/j.matlet.2021.129700.

[55] P. Ilg, M. Kröger, Dynamics of interacting magnetic nanoparticles: effective behavior from competition between brownian and néel relaxation, Phys. Chem. Chem. Phys 22 (2020) 22244–22259. doi:10.1039/d0cp04377j.